Surface-facet-dependent phonon deformation potential in individual strained topological insulator Bi_2Se_3 nanoribbons

Surface-Facet-Dependent Phonon Deformation Potential in Individual Strained Topological Insulator Bi$_2$Se$_3$ Nanoribbons

Yuan Yan,[§,†,*] Xu Zhou,[#,±,†] Han Jin,[#,†] Cai-Zhen Li,[#] Xiaoxing Ke,[Δ] Gustaaf Van Tendeloo,[Δ] Kaihui Liu,[#, ‡ ,±] Dapeng Yu,[#,‡ ,±] Martin Dressel,[§] and Zhi-Min Liao[#, ‡ ,*]

[§]1. Physikalisches Institut, Universität Stuttgart, 70550 Stuttgart, Germany, [#]State Key Laboratory for Mesoscopic Physics, Department of Physics, Peking University, 100871 Beijing, China, [±]Academy for Advanced Interdisciplinary Studies, Peking University, 100871 Beijing, China, [Δ]EMAT (Electron Microscopy for Materials Science), University of Antwerp, Groenenborgerlaan 171, B-2020 Antwerp, Belgium, [‡] Collaborative Innovation Center of Quantum Matter, Beijing, China

[†]These authors contributed equally to this work

[*]Address correspondence to yuan.yan@pi1.physik.uni-stuttgart.de; liaozm@pku.edu.cn

ABSTRACT Strain is an important method to tune the properties of topological insulators. For example, compressive strain can induce superconductivity in Bi$_2$Se$_3$ bulk material. Topological insulator nanostructures are the superior candidates to utilize the unique surface states due to the large surface to volume ratio. Therefore, it is highly desirable to monitor the local strain effects in individual topological insulator nanostructures. Here, we report the systematical micro-Raman spectra of single strained Bi$_2$Se$_3$ nanoribbons with different thicknesses and different surface facets, where four optical modes are resolved in both Stokes and anti-Stokes Raman spectral lines. A striking anisotropy of the strain dependence is observed in the phonon frequency of strained Bi$_2$Se$_3$ nanoribbons grown along the <11$\bar{2}$0> direction. The frequencies of the

in-plane E_g^2 and out-of-plane A_{1g}^1 modes exhibit a nearly linear blue-shift against bending strain when the nanoribbon is bent along the $<11\bar{2}0>$ direction with the curved {0001} surface. In this case, the phonon deformation potential of the E_g^2 phonon for 100 nm-thick Bi$_2$Se$_3$ nanoribbon is up to 0.94 cm^{-1}/%, which is twice of that in Bi$_2$Se$_3$ bulk material (0.52 cm^{-1}/%). Our results may be valuable for the strain modulation of individual topological insulator nanostructures.
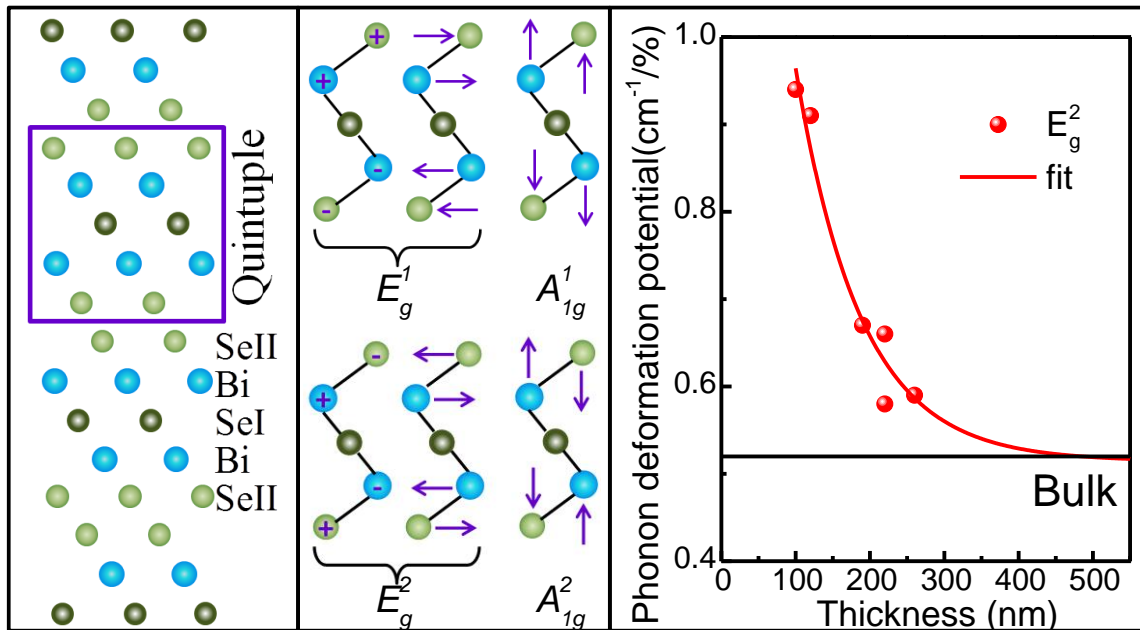
KEYWORDS: topological insulator, Bi$_2$Se$_3$ nanoribbon, Raman spectroscopy, strain, phonon confinement effect

Topological insulators (TIs) are a new class of quantum matter that possess a trivial insulating bulk phase and robust non-trivial metallic surface states.[1-5] They are considered as promising candidates for novel electronic applications beyond silicon in current electronic world, attracting enormous efforts from both theoretical and experimental research. Among the TIs family, Bi$_2$Se$_3$ has been proven to be an ideal candidate for

studying topological surface states due to its simple energy band structure and relatively large bulk band gap of ~ 0.3 eV.[6] The pressure induced phase transition from non-superconducting to superconducting phases in topological insulator Bi_2Se_3,[7-8] Bi_2Te_3[9-10] and Sb_2Te_3[11] bulk materials have been reported, however, ultrahigh pressure is required and a full understanding of the interplay between superconductivity and topological surface states is still elusive.[12-13] Compared to bulk materials, nanostructures have higher crystalline quality, surface-to-volume ratio, and elastic limit[14-15] and thus are more favorable to realize topological superconductivity and to investigate the Majorana fermions.[16-17] However, to our best knowledge, the influence of size, strain and facet on the physical properties of strained Bi_2Se_3 nanoribbons has not been studied yet.

Micro-Raman spectroscopy is well established as a powerful and sensitive technique to characterize graphene-like layer materials.[18-24] Substrate,[25-27] thickness[28-29] and doping level[30-31] dependent $in\ situ$ and $ex\ situ$ Raman spectra of Bi_2Se_3 ultra-thin film and nanoplate have been reported. In this work we report the strain, thickness and surface facet dependent phonon properties in individual Bi_2Se_3 nanoribbons. Utilizing the ultrafine glass tip of a micromanipulator we strained tens of Bi_2Se_3 nanoribbons with thicknesses ranging from 70 nm to 500 nm. For a typical strain-free Bi_2Se_3 nanoribbon, all the four optical modes, the in-plane E_g^1 and E_g^2 modes and the out-of-plane A_{1g}^1 and A_{1g}^2 modes, are resolved in both Stokes and anti-Stokes Raman spectra. As expected, these modes soften with decreasing thickness, which is consistent with theoretical predictions.[25-26, 28, 32] Besides that, a strong anisotropic behavior is observed for bent Bi_2Se_3 nanoribbon, due to the two structurally different facets, the {0001} and the {01$\bar{1}$5} surface, of Bi_2Se_3 nanoribbons grown along the <11$\bar{2}$0> direction.[33-36] Only when the

nanoribbon is bent along the $<11\bar{2}0>$ direction with the curved {0001} surface perpendicular to the substrate plane and with the exposed {01$\bar{1}$5} top surface, the frequencies of in-plane E_g^2 and out-of-plane A_{1g}^1 modes exhibit a linear blue-shift with increasing strain, which is also strongly thickness dependent. The phonon deformation potential (PDP) of the E_g^2 mode is up to 0.94 cm^{-1}/% for 100 nm-thick Bi_2Se_3 nanoribbon, while it is only approximately 0.52 cm^{-1}/% for Bi_2Se_3 bulk material.[37] Since the phonon modes stiffen linearly as the lattice is compressed,[37-38] the properties of the Bi_2Se_3 nanoribbons are more sensitive to strain than that of bulk materials. Our work indicates that thin Bi_2Se_3 nanoribbons are a promising candidate to study the strain modulated unique properties of the topological surface states.

RESULTS AND DISCUSSION

Raman spectrum of unstrained Bi_2Se_3 nanoribbon. Bi_2Se_3 nanoribbons were synthesized by the Chemical Vapor Deposition (CVD) method,[39] and their thickness ranges from 70 to 500 nm while the length from tens to hundreds of micrometers (Figures S1 and S2). The single crystalline nature of Bi_2Se_3 nanoribbons was confirmed by transmission electron microscopy (TEM) (Figure S1(b)), high-resolution TEM (HRTEM) (Figure S1(c)) and selected area electron diffraction (SAED) patterns (Figure S1(d)). The growth direction of the Bi_2Se_3 nanoribbons is always along $<11\bar{2}0>$. Figures 1(a-c) show the scanning TEM (STEM) results of the cross-sectional sample of a nanoribbon, revealing the exposed facets of the as-grown nanoribbons. A TEM image of a representative cross-sectional sample is shown in Figure 1(b) at low magnification, and its side facet indicated by the blue box is enlarged in Figure 1(a) by a high resolution

high-angle annular dark field (HAADF) STEM image. The Fast Fourier Transformation (FFT) pattern of Figure 1(a) is shown in Figure 1(c), which reveals the two structurally inequivalent types of facets to be the $\{0001\}$ and the $\{01\bar{1}5\}$ surfaces.[35-36] Consequently, there are two possibilities to position the Bi_2Se_3 nanoribbons on the substrate: with the $\{0001\}$ surface parallel to the substrate plane (Figure 1(d)), or with the $\{01\bar{1}5\}$ surface parallel to the substrate (Figure 1(e)). Correspondingly, the nanoribbons can be bent in two different geometries. Later, we will discuss the Raman spectra of these two kinds of bent Bi_2Se_3 nanoribbons with different thicknesses. Surprisingly they exhibit a totally different strain response.

Bi_2Se_3 has a layered rhombohedral structure, which belongs to the space group D_{3d}^5 ($R\bar{3}m$) as shown in Figure 2(a). Each unit cell includes five atomic layers in the sequence of SeII-Bi-SeI-Bi-SeII, which is often referred as quintuple layer (QL) with a dimension of ~1 nm along c axis. Stacks of QLs linked by weak van der Waals forces with a slightly covalent nature, while intra QL possess strong covalent bonds. Considering the symmetry of the space group D_{3d}^5, the primitive unit cell contains five atoms corresponding to the chemical formula of Bi_2Se_3. Accordingly, there are 15 lattice dynamical modes at the center of its Brillouin zone (q=0), three of which are acoustic and 12 are optical modes. These 12 optical modes can be classified by the irreducible representations $\chi = 2E_g + 2A_{1g} + 2E_u + 2A_{1u}$.[32] According to the selection rules, $2A_{1u}$ and $2E_u$ are infrared-active, while $2A_{1g}$ and $2E_g$ are Raman-active modes.[31] The Raman tensors of the latter one are[31]

$$A_{1g}: \begin{pmatrix} a & 0 & 0 \\ 0 & a & 0 \\ 0 & 0 & b \end{pmatrix},$$

$$E_g: \begin{pmatrix} c & 0 & 0 \\ 0 & -c & d \\ 0 & d & 0 \end{pmatrix}, \begin{pmatrix} 0 & -c & -d \\ -c & 0 & 0 \\ -d & 0 & 0 \end{pmatrix}. \tag{1}$$

The intensity of Raman scattering $I \sim |e_s \cdot R \cdot e_i|^2$ may be different for the $\{01\bar{1}5\}$ or the $\{0001\}$ surface perpendicular to the direction of incident light, where e_s and e_i represent the unit polarization vectors of scattered and incident light, respectively, and are related to the orientation of the sample.

The corresponding atomic displacements of the Raman-active modes are depicted in Figure 2(b), where the E_g modes are twofold in-plane vibrational modes and the A_{1g} modes vibrating along the [0001] direction are out-of-plane modes. These two types of Raman-active modes can be distinguished by the nonzero off-diagonal components in the E_g Raman tensor. In Figure 2(c) a typical unpolarized Raman spectrum of an unstrained Bi$_2$Se$_3$ nanoribbon is plotted consisting of both Stokes and anti-Stokes contributions. All four bulk vibrational modes E_g^1, A_{1g}^1, E_g^2 and A_{1g}^2 are observed, with the corresponding peak positions at 37.3, 70.4, 131.9 and 171.2 cm^{-1}. In order to determine the Raman peak position and the line width, all the Raman spectra are fitted by Lorentzian lineshape.

Strain dependent Raman spectra of Bi$_2$Se$_3$ nanoribbons with the $\{0001\}$ surface parallel to the substrate plane. In order to investigate the influence of strain on the physical properties of topological insulator Bi$_2$Se$_3$ nanoribbons, a series of samples with various thickness and width are bent and measured. Figure 3(a) shows the scanning electron microscopy (SEM) image and scheme of a typical bent Bi$_2$Se$_3$ nanoribbon. To distinguish a given nanoribbon was lying either with its $\{0001\}$ facets facing up and down on the substrate or the facets on the other long edge of the nanoribbon ($\{01\bar{1}5\}$)

facing up and down, the sample was characterized by atomic force microscopy (AFM) to get the thickness and width. The width of this nanoribbon is 300 nm and the thickness is 180 nm. According to the STEM results, tens more cross-sectional Bi_2Se_3 nanoribbon samples with different sizes had been prepared, and we found – without an exception – the width of the samples is always larger than the thickness, which implies that the {0001} facets are bigger than the {01$\bar{1}$5} facets. This can be easily understood by the growth mechanism. Because Bi_2Se_3 is a layered material, the in-plane growth is much easier than the growth along [0001] direction. For this sample shown in Figure 3(a), the Bi_2Se_3 nanoribbon should be with the {0001} surface parallel to the substrate plane. Raman spectra collected from three different positions along the Bi_2Se_3 nanoribbon, marked by red, green and blue color in Figure 3(a), are shown in Figure 3(b) plotted with respective color. The frequencies of all four vibrational peaks E_g^1, A_{1g}^1, E_g^2 and A_{1g}^2 are denoted by the dashed lines.

Quantitatively, the maximum tensile and compressive strain ε_{ab}^{max} at the outer and inner side of the bent Bi_2Se_3 nanoribbon can be calculated by[40]

$$\varepsilon_{ab}^{max} = \frac{a-a_0}{a_0} = \pm\frac{d}{2R_{ab}}, \tag{2}$$

where a and a_0 are the lattice constants of the sample in the strained and unstrained case, d is the width of the Bi_2Se_3 nanoribbon here, and R_{ab} is the radius of curvature with $R = \frac{[1+(f')^2]^{\frac{3}{2}}}{|yf''|}$, where $y = f(x)$ is the curve function of bent Bi_2Se_3 nanoribbon. When the bending strain increases from 0 to 2.4%, the frequencies of all four vibrational modes E_g^1, A_{1g}^1, E_g^2 and A_{1g}^2 remain constant (Figure 3(c)). The full width at half maximum

(FWHM) of the in-plane E_g^2 peak exhibits a negligible increase from 6 to 8 cm^{-1} with increasing strain, while the ratio of Raman intensities $I_{A_{1g}^1}/I_{A_{1g}^2}$ does not change (Figure 3(d)). Considering the much larger spot size (~1 μm) of incident laser compared to the width of the nanoribbon, the contributions from the tensile outer side and the compressive inner side of the narrow nanoribbon will add up and cancel the frequency shift, as well as induce the broadening of the FWHM of the E_g^2 mode. As there is no strain along the [0001] direction in this case, the Raman intensity of the out-of-plane modes does not change with the bending strain ε_{ab}. Similar results of three more samples are shown in Figure S3-S5 in the supporting information.

Strain dependent Raman spectra of Bi$_2$Se$_3$ nanoribbons with the exposed {01$\bar{1}$5} top surface on the substrate. A typical SEM image and scheme of a bent 100 nm-thick Bi$_2$Se$_3$ nanoribbon are produced in Figure 4(a), where the {0001} surface is perpendicular to the substrate plane and the exposed top surface is the {01$\bar{1}$5} surface. The nanoribbon is bent along the <11$\bar{2}$0> direction with the curved {0001} surface. The Raman spectra are fitted by Lorentzian lineshape and plotted in Figure 4(b). Five curves with different colors correspond to the five positions on the Bi$_2$Se$_3$ nanoribbon marked by the same colors in Figure 4(a). With increasing strain, the Raman frequencies of the A_{1g}^1 and E_g^2 features rise linearly, similar with the typical pressure-induced phonon stiffening[37]. The shear stress along c direction enhances the bond interaction by decreasing the bond length of Bi-SeI and SeII-SeII, resulting in the blue shift of the vibrational frequencies of the A_{1g}^1 and E_g modes. The corresponding PDP of these two modes are about 0.66 and 0.94 cm^{-1}/%, respectively (Figure 4(c)).

For a comparison, the reported PDP of the E_g^2 mode in bulk Bi_2Se_3 material under pressure (3.13 cm^{-1}/GPa) [37] can be converted to a strain value (%) by[40]

$$\frac{\partial \Delta \omega}{\partial \varepsilon} = (1 - 2\upsilon) E_{ab} \frac{\partial \Delta \omega}{\partial \sigma_{ab}}, \tag{3}$$

The Poisson's ratio υ used here is 0.27, and the value of Young's modulus of Bi_2Se_3 bulk material along the <11$\bar{2}$0> direction E_{ab} is 35.9 GPa,[41] thus the PDP of bulk material is 0.52 cm^{-1}/%. It is worth noting that the frequency shift of the E_g^2 mode induced by the same strain in the Bi_2Se_3 nanoribbon is nearly twice of what is observed in bulk. In contrast to the blue-shift of the A_{1g}^1 and E_g^2 modes, the Raman frequencies of the A_{1g}^2 peak exhibit a red-shift with the PDP value about -1.78 cm^{-1}/%. The red-shift of the out-of-plane A_{1g}^2 mode may be caused by the strain modulation of the opposite vibrations of the Bi and SeII atoms. [28] The FWHM of both A_{1g}^1 and E_g^2 modes remains almost unchanged, implying that the phonon-phonon scattering stays the same (Figure 4(d)). Usually, the vibrational peaks broaden when contributions from tensile strain at outer surface and compressive strain at inner surface add up. On the other hand, the FWHM decreases when the strain-induced carrier concentration rises.[19] It has been reported that the carrier concentration of Bi_2Se_3 bulk materials is enhanced more than ten times when the pressure increases from 0 to 10 GPa,[7] even without a structural phase transition. We conclude that the FWHM of both A_{1g}^1 and E_g^2 modes is unaltered as these two opposite effects cancel each other.

A series of bent Bi_2Se_3 nanoribbons with different thicknesses have been measured (Figures S6 and S7). As shown in Figure 5(a), the Raman shift of the E_g^2 modes in 100,

120, 190, 220 and 260 nm-thick Bi_2Se_3 nanoribbons all exhibit a blue-shift with increasing strain. Some deviations from the linear relationship may be caused by the nonuniform interaction between Bi_2Se_3 nanoribbons and the substrate. The most interesting discovery is that the PDP of the E_g^2 feature increases with reducing the sample thickness (Figure 5(b)), which may arise from the surface effect.[14] Therefore, the strain modification on the phonon properties depends on the thickness of the Bi_2Se_3 nanoribbons strongly. As reported, the relationship between the FWHM and thickness had been explained using exponential format.[32] Similarly, here we also use the exponential fit to thickness dependence of the PDP of E_g^2 mode in Figure 5(b).

Thickness dependent Raman spectra of strain-free Bi_2Se_3 nanoribbons. To explore the size effect in topological insulators, Raman spectra of three dimensional (3D) bulk materials and 2D thin films have been collected,[3, 25, 28-29, 32] where infrared features were observed due to the symmetry breaking in 2D thin film samples.[29, 42] Here, quasi 1D Bi_2Se_3 nanoribbons with various thicknesses are measured to further investigate the size effect.

In Figure 6(a), the Raman peak positions of individual Bi_2Se_3 nanoribbons are plotted as a function of the sample thickness. When the thicknesses d of unstrained Bi_2Se_3 nanoribbons decreases from 500 to 70 nm, the frequencies of both A_{1g}^1 and E_g^2 modes exhibit a red-shift about 4 cm^{-1}, which is consistent with previous results of thin film materials.[25, 28, 32, 43] Considering the phonon confinement effects, the red-shift would relate to the surface-to-volume ratio, or $1/d$.[44, 45] Then the relationship of the frequency and d can be fitted by[32, 44]

$$\omega(d) = \omega(0) - A/d, \tag{4}$$

where $\omega(0)$ is the phonon frequency in the bulk (Figure 6(a)). Meanwhile, the surface relaxation and structural defects should also be considered to explain the red-shift.

The ratio of the Raman intensities $I_{A_{1g}^1}/I_{A_{1g}^2}$ increases as the thickness is reduced, in contrast to the results reported for thin films.[32] Considering the surface tension in the nanostructure with large surface-to-volume ratio, the strength of the out-of-plane vibration A_{1g}^1 mode should be enhanced by decreasing thickness, as shown in Figure 6(b).

Discussion. Our systematic investigations of the strain, thickness and surface facet dependent Raman spectra of Bi_2Se_3 nanoribbons yield the basis for some important points. For strain-free samples, all the optical phonon frequencies become red-shifted as the sample thickness is reduced, due to the increased phonon confinement effect and surface tension, which is insensitive to the way how the nanoribbons are placed on the substrate. While for strained samples with the $\{0001\}$ or the $\{01\bar{1}5\}$ surface parallel to the substrate plane, strong anisotropies are observed, caused by the different bending loading method on the nanoribbon. The strain induced anisotropy demonstrates that Raman spectra of Bi_2Se_3 nanoribbon are more sensitive to the stress along c direction. Furthermore, the PDP of the E_g^2 mode of Bi_2Se_3 nanoribbon was found to increase with decreasing the nanoribbon thickness. Therefore, a much lower critical pressure (stress) is expected to be sufficient to induce a superconducting phase transition in thin Bi_2Se_3 nanoribbons compared to the bulk counterpart. Utilizing this great advantage of nanostructures, a superconducting dome was observed recently in WTe_2 nanoflakes with a pressure even smaller than 5 Gpa.[46]

CONCLUSIONS

In conclusion, the influence of size and strain on the Raman spectra of topological insulator Bi_2Se_3 nanoribbons are investigated systematically. All four optical modes, the in-plane E_g^1 and E_g^2, and out-of-plane A_{1g}^1 and A_{1g}^2 modes, are resolved in both Stokes and anti-Stokes Raman spectra, and they all soften as the thickness of unstrained Bi_2Se_3 nanoribbons reduces. While for bent Bi_2Se_3 nanoribbons a strong anisotropy is observed, due to the differences in the exposed top facets on the substrate: the {0001} and the {01$\bar{1}$5} surfaces. Only when the {0001} surface is perpendicular to the substrate plane and the exposed top surface is the {01$\bar{1}$5} surface, that is, the nanoribbon is bent along the <11$\bar{2}$0> direction with the curved {0001} surface, the E_g^2 and A_{1g}^1 (A_{1g}^2) modes of the Bi_2Se_3 nanoribbon show a blue-shift (red-shift) with strain, and the phonon deformation potential of the E_g^2 mode rises nonlinearly with decreasing sample thickness. The results are helpful for further investigations on the quantum transport of strained Bi_2Se_3 nanostructures.

MATERIALS AND METHODS

Synthesis of Bi_2Se_3 Nanoribbons. Bi_2Se_3 nanoribbons were synthesized by CVD method. Bi_2Se_3 powder (Alfa Aesar) with high purity (> 99.99%) was put in the center of a horizontal tube furnace (Lindberg/Blue M) as the source, while several undoped silicon pieces with 5 nm gold film deposited by electron beam evaporation were placed downstream approximately 9 cm away from the source as the collecting substrates. High purity Ar gas was used to pump and flush the tube, maintain the inside pressure and carry the source vapor from central hot zone (700 °C) to the cold edge (about 350 °C). After

the growth, desirable Bi_2Se_3 nanoribbons were chose from the as-grown products, transferred onto the Si/SiO_2 substrate with marks, and then manipulated to be curved under an optical microscope with micromanipulator by using two needle-shaped glass tips.

Characterization of Bi_2Se_3 Nanoribbons. The as-synthesized Bi_2Se_3 nanoribbons were characterized by the field-emission SEM (FEI NanoSEM 430) with the accelerating voltage 10 kV. The Bi_2Se_3 nanoribbons were transferred onto a copper grid by gently rub it on an as-grown substrate and then characterized by 200 kV field-emissions TEM (Tecnai G2 F20). To prepare the cross-sectional TEM sample, ten more Bi_2Se_3 nanoribbons were transferred onto $SrTiO_3$ substrate. The nanoribbons were randomly chosen using focused ion beam (FIB, FEI Helios NanoLab DualBeam system). Amorphous carbon/Pt protection layer was deposited to protect the Bi_2Se_3 nanoribbon surface by electron beam induced deposition method in the FIB system. Then, the Bi_2Se_3 nanoribbon was cut along the cross-section by the FIB and then transferred onto a TEM grid by a nano-manipulator in the FIB system. HAADF-STEM was performed using an FEI Titan Cube 60-300 microscope fitted with an aberration corrector for the probe forming lens operated at 200 kV.

Raman Spectral Measurement. Unpolarized Raman spectra of the Bi_2Se_3 nanoribbons were measured by a home-built confocal micro-Raman microscopy system (Princeton Instruments Acton SP 2500 i) in the backscattering configuration at room temperature. The Raman spectra are excited by a λ=532 nm solid state laser with high power stability. The focused spot size is about 1 μm, the spectra resolution ~1 cm^{-1} and the lowest available frequency is better than 20 cm^{-1} by a set of 532 nm BragGrate™

Notch Filter (532 BNF). The incident laser power after the 100x objective (N.A. = 0.90) is about 0.2 mW to avoid sample damage or laser induced heating. Each spectrum is collected for 3 minutes, because the signal of the nanoribbon is relatively small.

Conflict of Interest: The authors declare no competing financial interest.

Supporting Information Available: SEM picture of as-synthesized Bi_2Se_3 nanoribbons. Typical TEM, HRTEM images and SAED patterns of a strain-free Bi_2Se_3 nanoribbon. Typical AFM image of a strained Bi_2Se_3 nanoribbon. Raman spectra of strained Bi_2Se_3 nanoribbons with different thicknesses in two cases. This material is available free of charge *via* the Internet at http://pubs.acs.org.

References

1. Fu, L.; Kane, C. L.; Mele, E. J. Topological Insulators in Three Dimensions. *Phys. Rev. Lett.* **2007,** *98*, 106803.
2. Kane, C. L.; Mele, E. J. Quantum Spin Hall Effect in Graphene. *Phys. Rev. Lett.* **2005,** *95*, 226801.
3. Moore, J. E.; Balents, L. Topological Invariants of Time-Reversal-Invariant Band Structures. *Phys. Rev. B* **2007,** *75*, 121306(R).
4. Qi, X.-L.; Zhang, S.-C. Topological Insulators and Superconductors. *Rev. Mod. Phys.* **2011,** *83*, 1057.
5. König, M.; Wiedmann, S.; Brüne, C.; Roth, A.; Buhmann, H.; Molenkamp, L. W.; Qi, X.-L.; Zhang, S.-C. Quantum Spin Hall Insulator State in HgTe Quantum Wells. *Science* **2007,** *318*, 766-770.
6. Zhang, H.; Liu, C.-X.; Qi, X.-L.; Dai, X.; Fang, Z.; Zhang, S.-C. Topological Insulators in Bi_2Se_3, Bi_2Te_3 and Sb_2Te_3 with a Single Dirac Cone on the Surface. *Nat. Phy.* **2009,** *5*, 438-442.
7. Kirshenbaum, K.; Syers, P.; Hope, A.; Butch, N.; Jeffries, J.; Weir, S.; Hamlin, J.; Maple, M.; Vohra, Y.; Paglione, J. Pressure-Induced Unconventional

Superconducting Phase in the Topological Insulator Bi_2Se_3. *Phys. Rev. Lett.* **2013,** *111*, 087001.

8. Zhao, J.; Liu, H.; Ehm, L.; Dong, D.; Chen, Z.; Gu, G. High-Pressure Phase Transitions, Amorphization, and Crystallization Behaviors in Bi_2Se_3. *J. Phys.: Cond. Matt.* **2013,** *25*, 125602.

9. Zhang, J.; Zhang, S.; Weng, H.; Zhang, W.; Yang, L.; Liu, Q.; Feng, S.; Wang, X.; Yu, R.; Cao, L*., et al.* Pressure-Induced Superconductivity in Topological Parent Compound Bi_2Te_3. *Proc. Natl. Acad. Sci.* **2011,** *108*, 24-28.

10. Zhang, C.; Sun, L.; Chen, Z.; Zhou, X.; Wu, Q.; Yi, W.; Guo, J.; Dong, X.; Zhao, Z. Phase Diagram of a Pressure-Induced Superconducting State and its Relation to the Hall Coefficient of Bi_2Te_3 Single Crystals. *Phys. Rev. B* **2011,** *83*, 140504.

11. Buga, S.; Kulbachinskii, V.; Kytin, V.; Kytin, G.; Kruglov, I.; Lvova, N.; Perov, N.; Serebryanaya, N.; Tarelkin, S.; Blank, V. Superconductivity in Bulk Polycrystalline Metastable Phases of Sb_2Te_3 and Bi_2Te_3 Quenched after High-Pressure–High-Temperature Treatment. *Chem. Phys. Lett.* **2015,** *631*, 97-102.

12. Levy, N.; Zhang, T.; Ha, J.; Sharifi, F.; Talin, A. A.; Kuk, Y.; Stroscio, J. A. Experimental Evidence for s-Wave Pairing Symmetry in Superconducting $Cu_xBi_2Se_3$ Single Crystals using a Scanning Tunneling Microscope. *Phys. Rev. Lett.* **2013,** *110*, 117001.

13. Hsieh, T. H.; Fu, L. Majorana Fermions and Exotic Surface Andreev Bound States in Topological Superconductors: Application to $Cu_x Bi_2Se_3$. *Phys. Rev. Lett.* **2012,** *108*, 107005.

14. Fu, X.-W.; Liao, Z.-M.; Liu, R.; Xu, J.; Yu, D. Size-Dependent Correlations between Strain and Phonon Frequency in Individual ZnO Nanowires. *ACS Nano* **2013,** *7*, 8891-8898.

15. van der Zande, A.; Hone, J. Optical Materials: Inspired by Strain. *Nat. Photon.* **2012,** *6*, 804-806.

16. Rokhinson, L. P.; Liu, X.; Furdyna, J. K. The Fractional ac Josephson Effect in a Semiconductor-Superconductor Nanowire as a Signature of Majorana Particles. *Nat. Phys.* **2012,** *8*, 795-799.

17. Mourik, V.; Zuo, K.; Frolov, S.; Plissard, S.; Bakkers, E.; Kouwenhoven, L. Signatures of Majorana Fermions in Hybrid Superconductor-Semiconductor Nanowire Devices. *Science* **2012,** *336*, 1003-1007.

18. Pisana, S.; Lazzeri, M.; Casiraghi, C.; Novoselov, K. S.; Geim, A. K.; Ferrari, A. C.; Mauri, F. Breakdown of the Adiabatic Born–Oppenheimer Approximation in Graphene. *Nat. Mater.* **2007,** *6*, 198-201.

19. Das, A.; Pisana, S.; Chakraborty, B.; Piscanec, S.; Saha, S.; Waghmare, U.; Novoselov, K.; Krishnamurthy, H.; Geim, A.; Ferrari, A*., et al.* Monitoring Dopants by Raman Scattering in an Electrochemically Top-Gated Graphene Transistor. *Nat. Nanotechnol.* **2008,** *3*, 210-215.

20. Coleman, J. N.; Lotya, M.; O'Neill, A.; Bergin, S. D.; King, P. J.; Khan, U.; Young, K.; Gaucher, A.; De, S.; Smith, R. J*., et al.* Two-Dimensional Nanosheets Produced by Liquid Exfoliation of Layered Materials. *Science* **2011,** *331*, 568-571.

21. Malard, L.; Pimenta, M.; Dresselhaus, G.; Dresselhaus, M. Raman Spectroscopy in Graphene. *Phy. Rep.* **2009,** *473*, 51-87.

22. Tan, P.; Han, W.; Zhao, W.; Wu, Z.; Chang, K.; Wang, H.; Wang, Y.; Bonini, N.; Marzari, N.; Pugno, N., *et al.* The Shear Mode of Multilayer Graphene. *Nat. Mater.* **2012,** *11*, 294-300.

23. Safdar, M.; Wang, Q.; Mirza, M.; Wang, Z.; Xu, K.; He, J. Topological Surface Transport Properties of Single-Crystalline SnTe Nanowire. *Nano Lett.* **2013,** *13*, 5344-5349.

24. Zhang, X.; Qiao, X.-F.; Shi, W.; Wu, J.-B.; Jiang, D.-S.; Tan, P.-H. Phonon and Raman Scattering of Two-Dimensional Transition Metal Dichalcogenides from Monolayer, Multilayer to Bulk Material. *Chem. Soc. Rev.* **2015,** *44*, 2757-2785.

25. Dang, W.; Peng, H.; Li, H.; Wang, P.; Liu, Z. Epitaxial Heterostructures of Ultrathin Topological Insulator Nanoplate and Graphene. *Nano Lett.* **2010,** *10*, 2870-2876.

26. Zhao, Y.; Luo, X.; Zhang, J.; Wu, J.; Bai, X.; Wang, M.; Jia, J.; Peng, H.; Liu, Z.; Quek, S. Y., *et al.* Interlayer Vibrational Modes in Few-Quintuple-Layer Bi_2Te_3 and Bi_2Se_3 Two-Dimensional Crystals: Raman Spectroscopy and First-Principles Studies. *Phys. Rev. B* **2014,** *90*, 245428.

27. Shahil, K.; Hossain, M.; Goyal, V.; Balandin, A. Micro-Raman Spectroscopy of Mechanically Exfoliated Few-Quintuple Layers of Bi_2Te_3, Bi_2Se_3, and Sb_2Te_3 Materials. *J. Appl. Phys.* **2012,** *111*, 054305.

28. Wang, C.; Zhu, X.; Nilsson, L.; Wen, J.; Wang, G.; Shan, X.; Zhang, Q.; Zhang, S.; Jia, J.; Xue, Q. *In situ* Raman Spectroscopy of Topological Insulator Bi_2Te_3 Films with Varying Thickness. *Nano Res.* **2013,** *6*, 688-692.

29. He, R.; Wang, Z.; Qiu, R. L.; Delaney, C.; Beck, B.; Kidd, T.; Chancey, C.; Gao, X. P. Observation of Infrared-Active Modes in Raman Scattering from Topological Insulator Nanoplates. *Nanotechnology* **2012,** *23*, 455703.

30. Soni, A.; Yanyuan, Z.; Ligen, Y.; Aik, M. K. K.; Dresselhaus, M. S.; Xiong, Q. Enhanced Thermoelectric Properties of Solution Grown $Bi_2Te_{3-x}Se_x$ Nanoplatelet Composites. *Nano Lett.* **2012,** *12*, 1203-1209.

31. Richter, W.; Becker, C. A Raman and Far-Infrared Investigation of Phonons in the Rhombohedral V2–VI3 Compounds Bi_2Te_3, Bi_2Se_3, Sb_2Te_3 and $Bi_2(Te_{1-x}Se_x)_3$ (0< x< 1), $(Bi_{1-y}Sb_y)_2Te_3$ (0< y< 1). *Phys. Stat. Sol. B* **1977,** *84*, 619-628.

32. Zhang, J.; Peng, Z.; Soni, A.; Zhao, Y.; Xiong, Y.; Peng, B.; Wang, J.; Dresselhaus, M. S.; Xiong, Q. Raman Spectroscopy of Few-Quintuple Layer Topological Insulator Bi_2Se_3 Nanoplatelets. *Nano Lett.* **2011,** *11*, 2407-2414.

33. Chen, F.; Jauregui, L.; Tan, Y.; Manfra, M.; Chen, Y.; Gerhard, K.; Kubis, T. In-Surface Confinement of Topological Insulator Nanowire Surface States. *arXiv:1505.04153*.

34. Yan, Y.; Liao, Z.-M.; Ke, X.; Van Tendeloo, G.; Wang, Q.; Sun, D.; Yao, W.; Zhou, S.; Zhang, L.; Wu, H.-C., *et al.* Topological Surface State Enhanced Photothermoelectric Effect in Bi_2Se_3 Nanoribbons. *Nano Lett.* **2014,** *14*, 4389-4394.

35. Yan, Y.; Wang, L.-X.; Ke, X.; Van Tendeloo, G.; Wu, X.-S.; Yu, D.-P.; Liao, Z.-M. High-Mobility Bi_2Se_3 Nanoplates Manifesting Quantum Oscillations of Surface States in the Sidewalls. *Sci. Rep.* **2014,** *4*, 3817.

36. Medlin, D.; Ramasse, Q.; Spataru, C.; Yang, N. Structure of the (0001) Basal Twin Boundary in Bi_2Te_3. *J. Appl. Phys.* **2010,** *108*, 043517.

37. Vilaplana, R.; Santamaría-Pérez, D.; Gomis, O.; Manjón, F.; González, J.; Segura, A.; Munoz, A.; Rodríguez-Hernández, P.; Pérez-González, E.; Marín-Borrás, V., *et*

al. Structural and Vibrational Study of Bi_2Se_3 under High Pressure. *Phys. Rev. B* **2011,** *84*, 184110.

38. Kong, P.; Zhang, J.; Zhang, S.; Zhu, J.; Liu, Q.; Yu, R.; Fang, Z.; Jin, C.; Yang, W.; Yu, X., *et al.* Superconductivity of the Topological Insulator Bi_2Se_3 at High Pressure. *J. Phys.: Cond. Matt.* **2013,** *25*, 362204.

39. Yan, Y.; Liao, Z.-M.; Zhou, Y.-B.; Wu, H.-C.; Bie, Y.-Q.; Chen, J.-J.; Meng, J.; Wu, X.-S.; Yu, D.-P. Synthesis and Quantum Transport Properties of Bi_2Se_3 Topological Insulator Nanostructures. *Sci. Rep.* **2013,** *3*, 1264.

40. Dietrich, C.; Lange, M.; Klüpfel, F.; Von Wenckstern, H.; Schmidt-Grund, R.; Grundmann, M. Strain Distribution in Bent ZnO Microwires. *Appl. Phys. Lett.* **2011,** *98*, 031105.

41. Koc, H.; Ozisik, H.; Deligöz, E.; Mamedov, A. M.; Ozbay, E. Mechanical, Electronic, and Optical Properties of Bi_2S_3 and Bi_2Se_3 Compounds: First Principle Investigations. *J. Mol. Model.* **2014,** *20*, 1-12.

42. Shahil, K.; Hossain, M.; Teweldebrhan, D.; Balandin, A. Crystal Symmetry Breaking in Few-Quintuple Bi_2Te_3 Films: Applications in Nanometrology of Topological Insulators. *Appl. Phys. Lett.* **2010,** *96*, 153103.

43. Hepting, M.; Kukuruznyak, D.; Benckiser, E.; Le Tacon, M.; Keimer, B. Raman Light Scattering on Ultra-Thin Films of $LaNiO_3$ under Compressive Strain. *Physica B* **2015,** *460*, 196-198.

44. Yang, C.; Li, S. Size-Dependent Raman Red Shifts of Semiconductor Nanocrystals. *J. Phys. Chem. B* **2008,** *112*, 14193-14197.

45. Adu, K.; Gutierrez, H.; Kim, U.; Sumanasekera, G.; Eklund, P. Confined Phonons in Si Nanowires. *Nano Lett.* **2005,** *5*, 409-414.

46. Pan, X.-C.; Chen, X.; Liu, H.; Feng, Y.; Song, F.; Wan, X.; Zhou, Y.; Chi, Z.; Yang, Z.; Wang, B., *et al.* Pressure-Induced Superconductivity in WTe_2. *arXiv:1501.07394*.

Figure Captions

Figure 1. Characterization of as grown Bi_2Se_3 nanoribbons. (a) High resolution HAADF-STEM image, (b) TEM image and (c) the corresponding FFT pattern of (a) from a cross-sectional sample of Bi_2Se_3 nanoribbon. High magnification SEM image of Bi_2Se_3 nanoribbon (d) with the {0001} surface and (e) with the {01$\bar{1}$5} surface lying on the substrate.

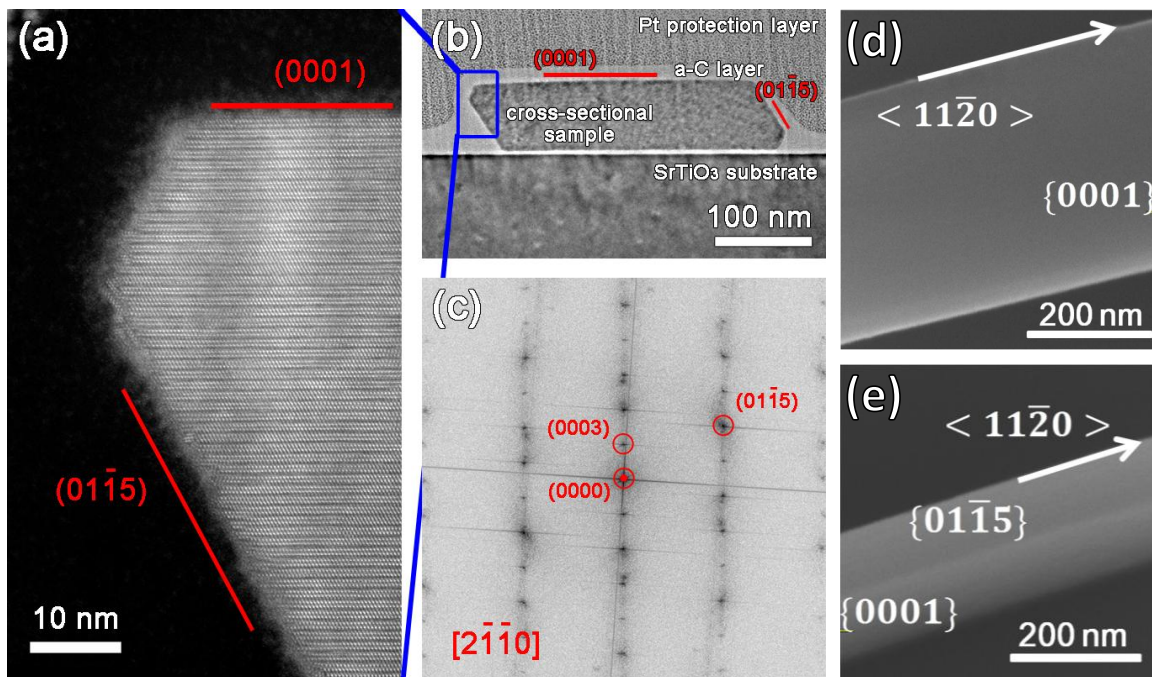Figure 2. Crystal structure and Raman modes of Bi_2Se_3. (a) Layered structure of Bi_2Se_3. Five atomic layers in sequence of SeII-Bi-SeI-Bi-SeII as a repeating unit along c axis are indicated. (b) Schematic illustration of atomic displacements of bulk Bi_2Se_3 in Raman-active modes, where "+" and "-" correspond to the inward and outward vibrations perpendicular to the paper plane, respectively. (c) Typical Raman spectrum of a strain-free Bi_2Se_3 nanoribbon consisting of both Stokes and anti-Stokes contributions, where all four bulk vibrational modes are observed and marked.
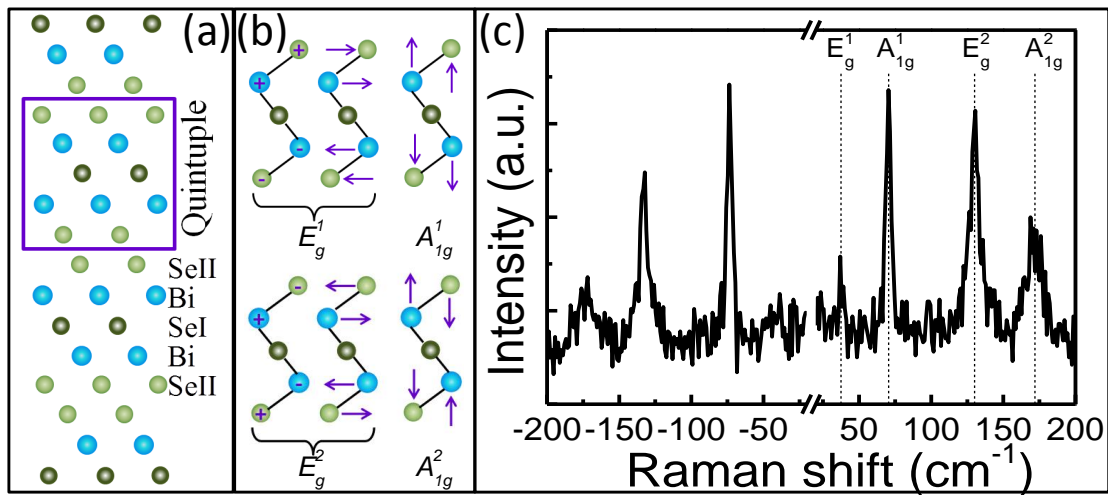
Figure 3. Raman spectra of a strained Bi_2Se_3 nanoribbon with the {0001} surface parallel to the substrate plane. (a) SEM image and schematic illustration of a bent Bi_2Se_3 nanoribbon with a width of 300 nm and a thickness of 180 nm. The nanoribbon is bent along the <11$\bar{2}$0> direction with the bending plane perpendicular to the {0001} surface. (b) Raman spectra collected at different positions along the Bi_2Se_3 nanoribbon. The color of each curve corresponds to three different points on the Bi_2Se_3 nanoribbon. Frequencies of four vibrational modes are indicated by dashed lines. (c) Relationship of Raman shift of these four vibrational modes against strain. (d) FWHM of E_g^2 mode and ratio of intensities $I_{A_{1g}^1}/I_{A_{1g}^2}$ as a function of strain.
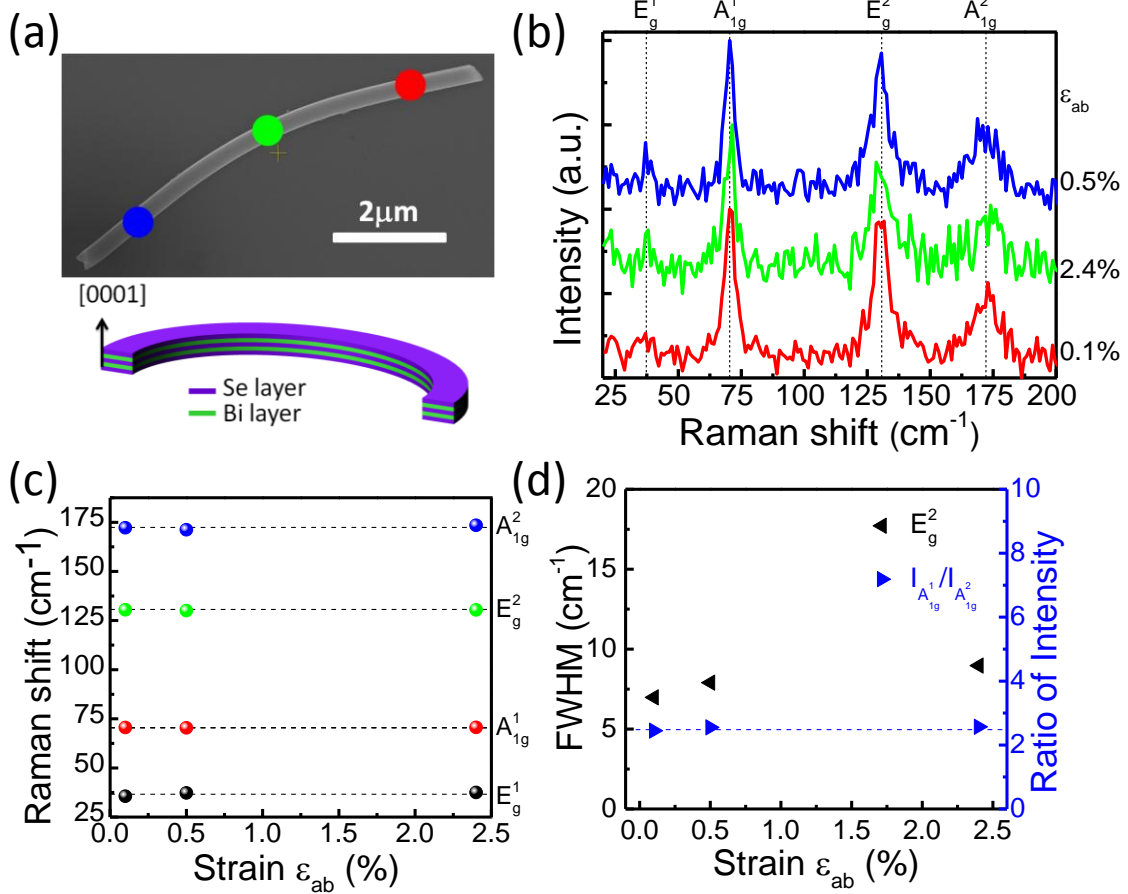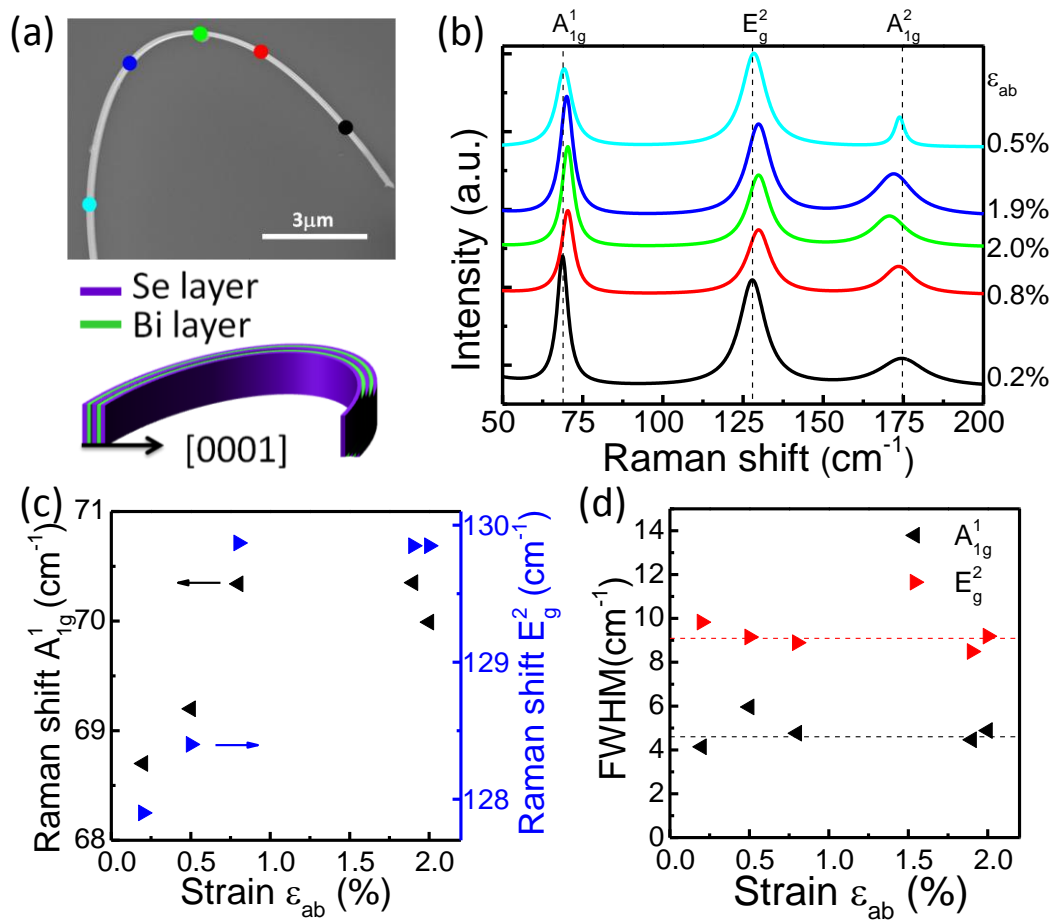
Figure 4. Raman spectra of a strained Bi_2Se_3 nanoribbon with the $\{0001\}$ surface perpendicular to the substrate plane and the exposed $\{01\bar{1}5\}$ top surface. (a) SEM image and schematic illustration of a bent Bi_2Se_3 nanoribbon with a thickness of 100 nm. The nanoribbon is bent along the $<11\bar{2}0>$ direction with the curved $\{0001\}$ surface. (b) Lorentzian fitted Raman spectra collected at different positions along the Bi_2Se_3 nanoribbon. The color of each curve corresponds to the five different points on this Bi_2Se_3 nanoribbon. (c) Relationship of Raman shift of the A_{1g}^1 and E_g^2 modes against strain. (d) FWHM of the A_{1g}^1 and E_g^2 modes as a function of strain.

Figure 5. Thickness dependent Raman shift of strained Bi_2Se_3 nanoribbons with the $\{0001\}$ surface perpendicular to the substrate plane and the exposed $\{01\bar{1}5\}$ top surface. (a) Relationship of strain and Raman shift of E_g^2 modes of 100, 120, 190, 220, 260 nm thick Bi_2Se_3 nanoribbons, and the data have been shifted up by a constant value to make it clear. (b) The phonon deformation potential (PDP) of E_g^2 mode *versus* the thickness of Bi_2Se_3 nanoribbons. The red line is the fit by an exponential function. The bold black line indicates the PDP value of Bi_2Se_3 bulk material from ref. 37.
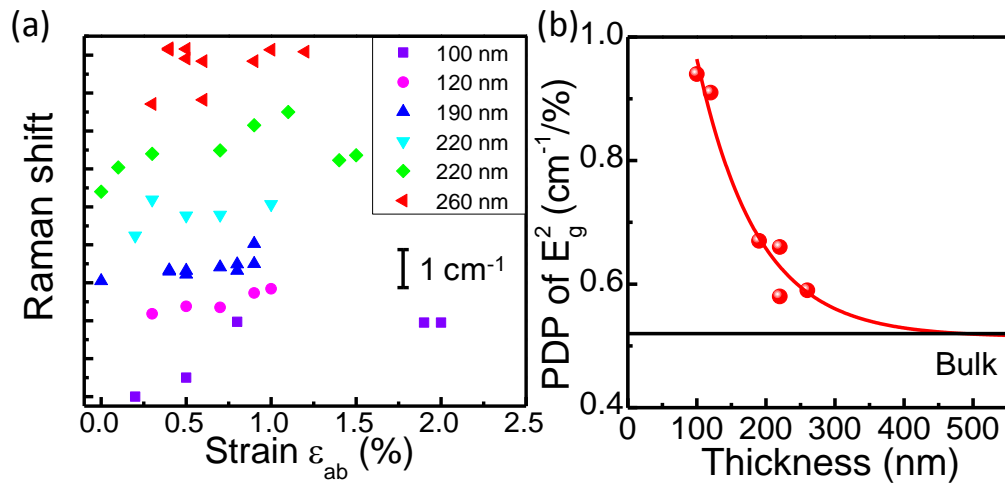
Figure 6. Thickness dependent Raman spectra of strain-free Bi_2Se_3 nanoribbons. (a) Raman shift of A_{1g}^1 and E_g^2 modes *versus* thickness. The black (red) solid line is fitting curve of A_{1g}^1 (E_g^2) mode. (b) Ratio of intensities $I_{A_{1g}^1}/I_{A_{1g}^2}$ *versus* thickness. The bold lines indicate the corresponding value of Bi_2Se_3 bulk material from ref. 31.

Surface-Facet-Dependent Phonon Deformation Potential in Individual Strained Topological Insulator Bi$_2$Se$_3$ Nanoribbons

Yuan Yan,[§,†,*] Xu Zhou,[#,±,†] Han Jin,[#,†] Cai-Zhen Li,[#] Xiaoxing Ke,[Δ] Gustaaf Van Tendeloo,[Δ] Kaihui Liu,[#, ‡ ,±] Dapeng Yu,[#,‡ ,±] Martin Dressel,[§] and Zhi-Min Liao[#, ‡ ,*]

[§]1. Physikalisches Institut, Universität Stuttgart, 70550 Stuttgart, Germany,

[#]State Key Laboratory for Mesoscopic Physics, Department of Physics, Peking University, 100871 Beijing, China,

[±]Academy for Advanced Interdisciplinary Studies, Peking University, 100871 Beijing, China,

[Δ]EMAT (Electron Microscopy for Materials Science), University of Antwerp, Groenenborgerlaan 171, B-2020 Antwerp, Belgium,

[‡] Collaborative Innovation Center of Quantum Matter, Beijing, China

[†]These authors contributed equally to this work

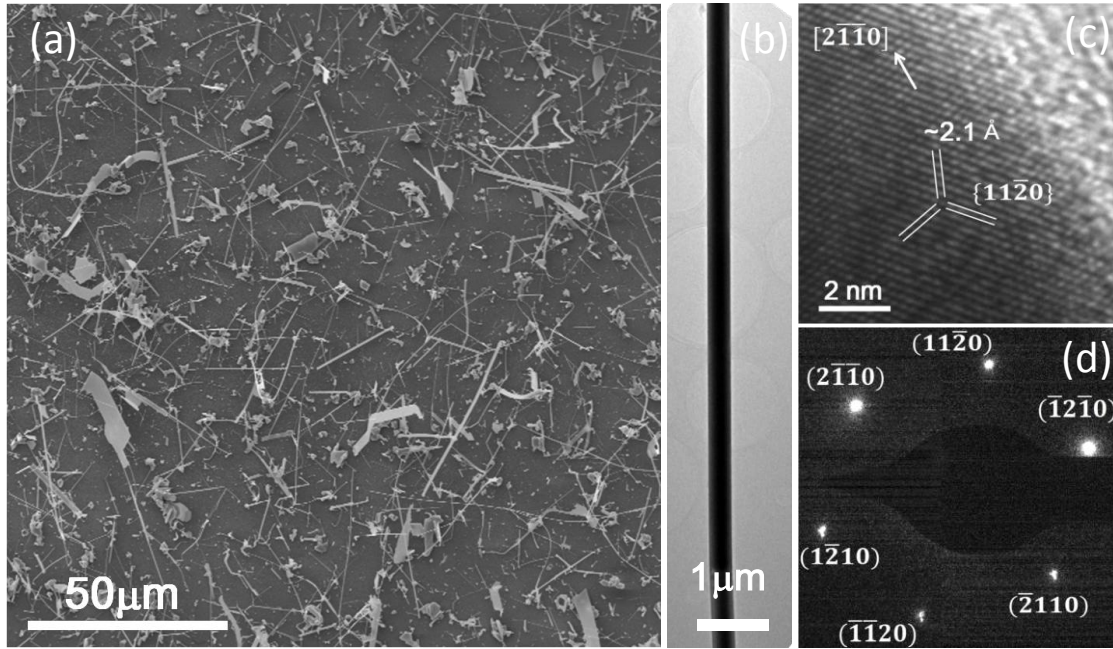[*]Address correspondence to yuan.yan@pi1.physik.uni-stuttgart.de; liaozm@pku.edu.cn

Figure S1. Characterization of as-grown Bi$_2$Se$_3$ nanoribbons. (a) SEM, (b) TEM, (c) HRTEM images and (d) SAED pattern of as grown Bi$_2$Se$_3$ nanoribbons.
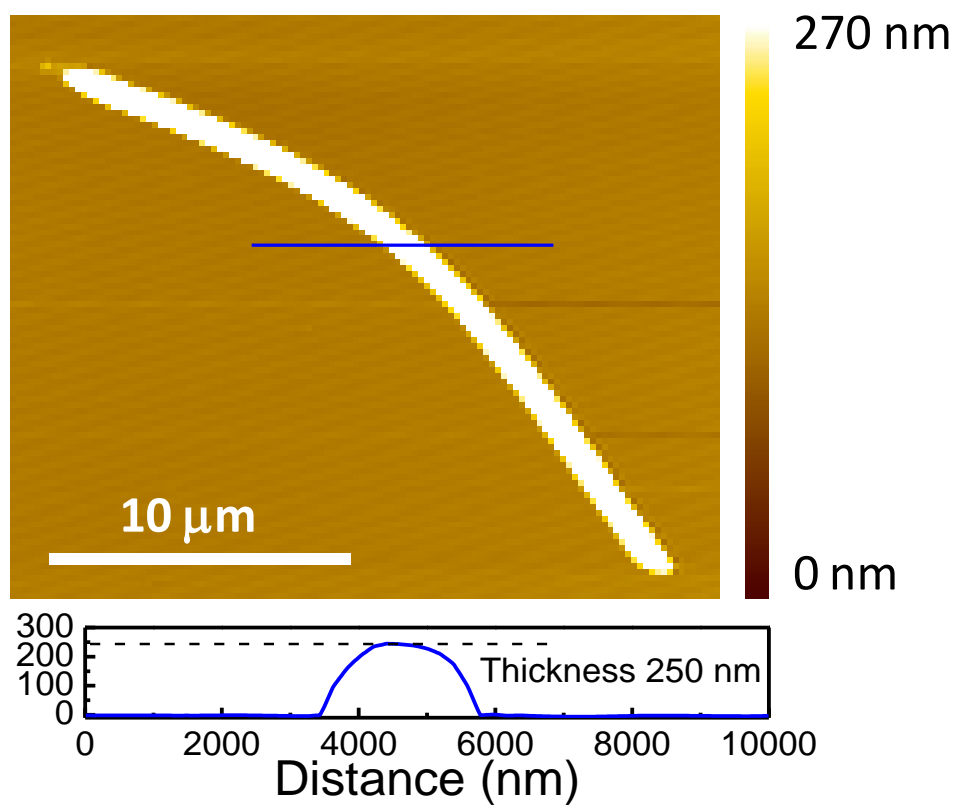
Figure S2. Atomic force microscopy (AFM) characterization of a representative Bi_2Se_3 nanoribbon after Raman measurements. The thickness is 250 nm.
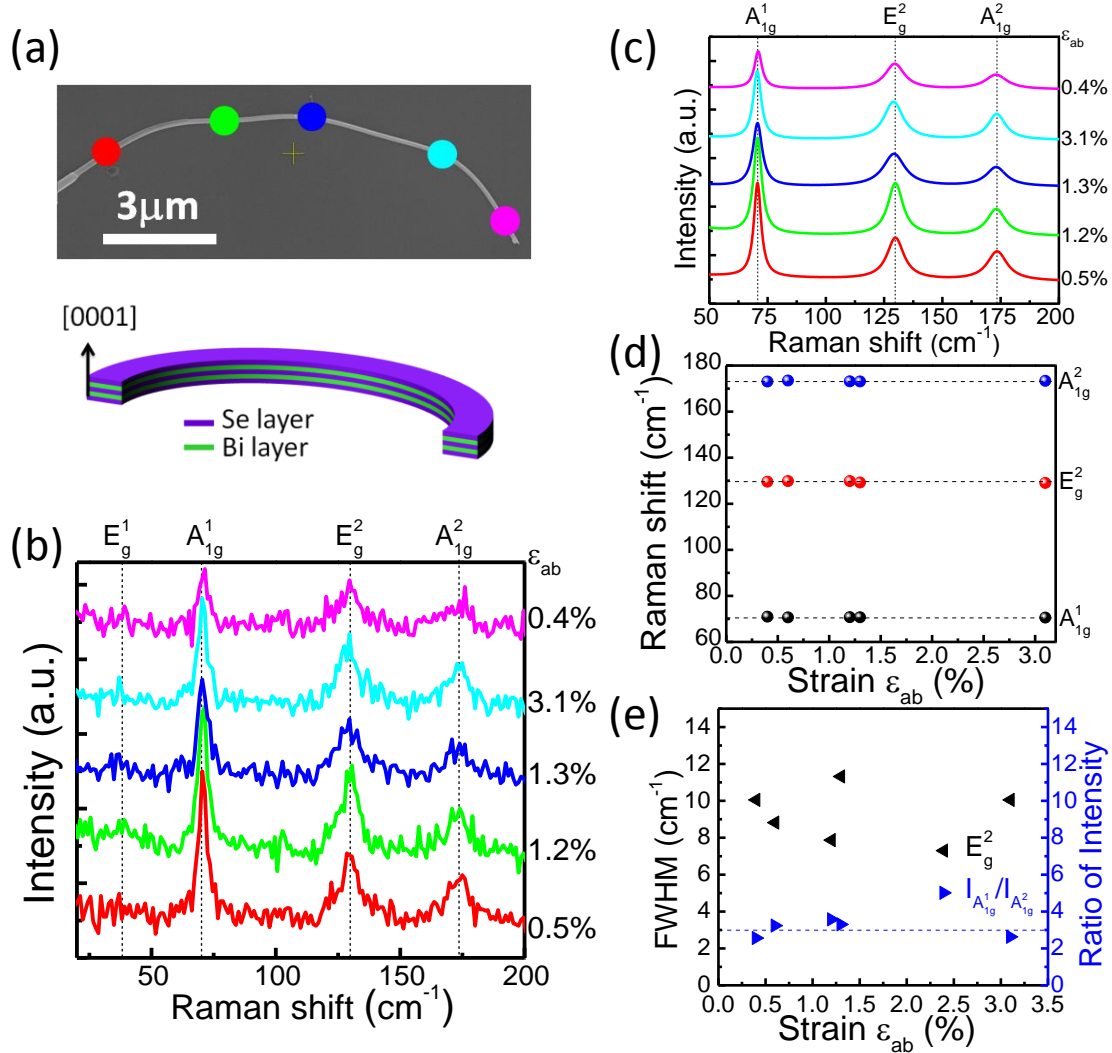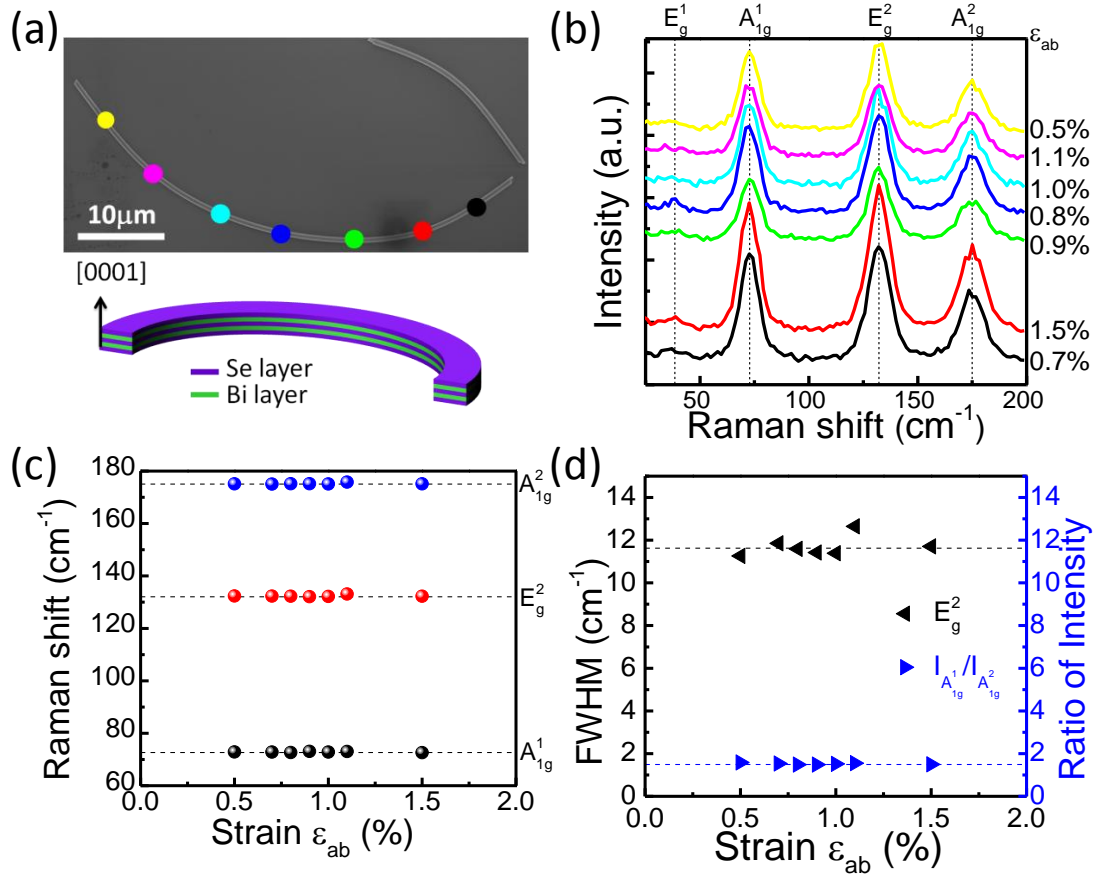
Figure S3. Raman spectra of a strained Bi_2Se_3 nanoribbon with the {0001} surface parallel to the substrate plane. (a) SEM image and schematic illustration of a bent Bi_2Se_3 nanoribbon with a width of 145 nm and a thickness of 130 nm. (b) Raman spectra and (c) Lorentzian fitted Raman spectra collected at different positions along the Bi_2Se_3 nanoribbon. The colored curves correspond to five different positions on the Bi_2Se_3 nanoribbon. Frequencies of the vibrational modes are indicated by dashed lines. (d) Raman shift of the vibrational modes (A_{1g}^1, E_g^2, A_{1g}^2) *versus* strain. (e) FWHM of E_g^2 mode and ratio of intensities $I_{A_{1g}^1}/I_{A_{1g}^2}$ as a function of strain.

Figure S4. Raman spectra of a strained Bi_2Se_3 nanoribbon with the {0001} surface parallel to the substrate plane. (a) SEM image and schematic illustration of a bent Bi_2Se_3 nanoribbon with a width of 320 nm and a thickness of 250 nm. (b) Raman spectra collected at different positions along the Bi_2Se_3 nanoribbon. The color of each curve corresponds to seven different points on the Bi_2Se_3 nanoribbon. Frequencies of each vibrational mode are indicated by dashed lines. (c) Raman shift of the vibrational modes (A_{1g}^1, E_g^2, A_{1g}^2) *versus* strain. (d) FWHM of E_g^2 mode and ratio of intensities $I_{A_{1g}^1}/I_{A_{1g}^2}$ as a function of strain.
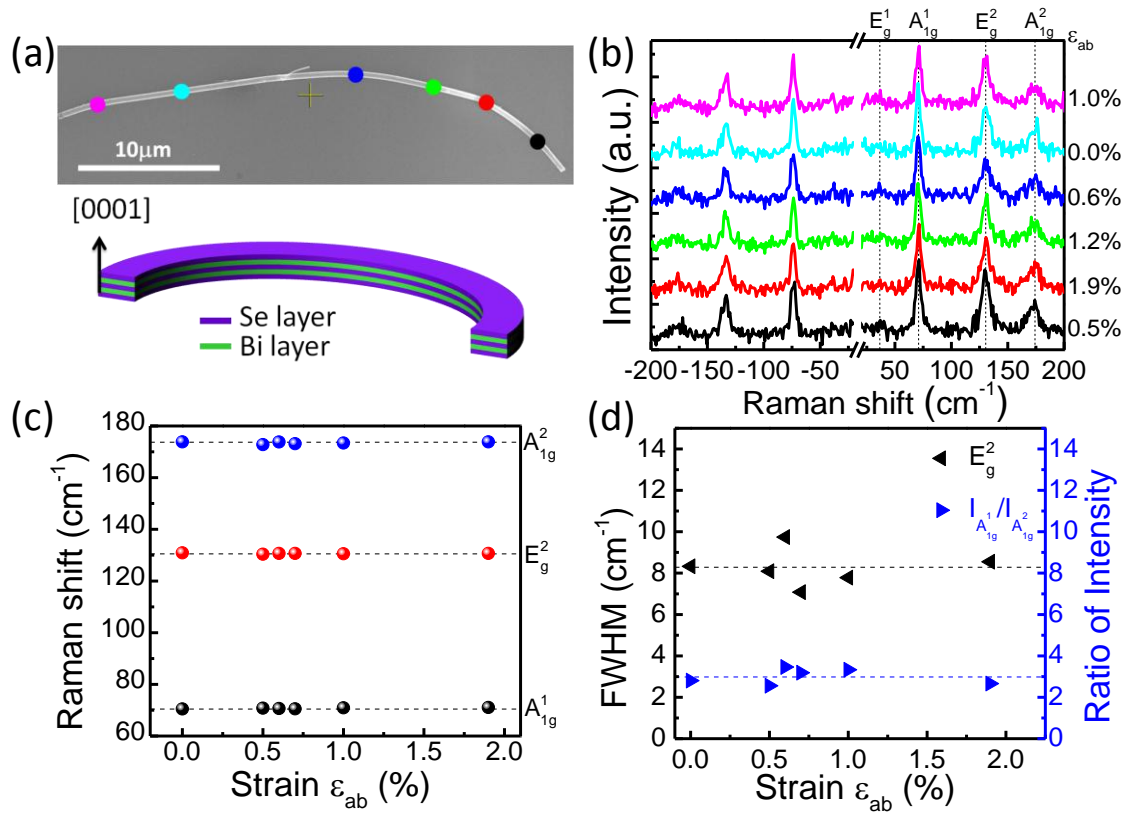
Figure S5. Raman spectra of a strained Bi₂Se₃ nanoribbon with the {0001} surface parallel to the substrate plane. (a) SEM image and schematic illustration of a bent Bi₂Se₃ nanoribbon with a width of 425 nm and a thickness of 170 nm. (b) Raman spectra collected at the different positions along the Bi₂Se₃ nanoribbon. The color of each curve corresponds to six different points on the Bi₂Se₃ nanoribbon. Frequencies of each vibrational mode are indicated by dashed lines. (c) Raman shift of the vibrational modes (A_{1g}^1, E_g^2, A_{1g}^2) *versus* strain. (d) FWHM of E_g^2 mode and ratio of intensities $I_{A_{1g}^1}/I_{A_{1g}^2}$ as a function of strain.
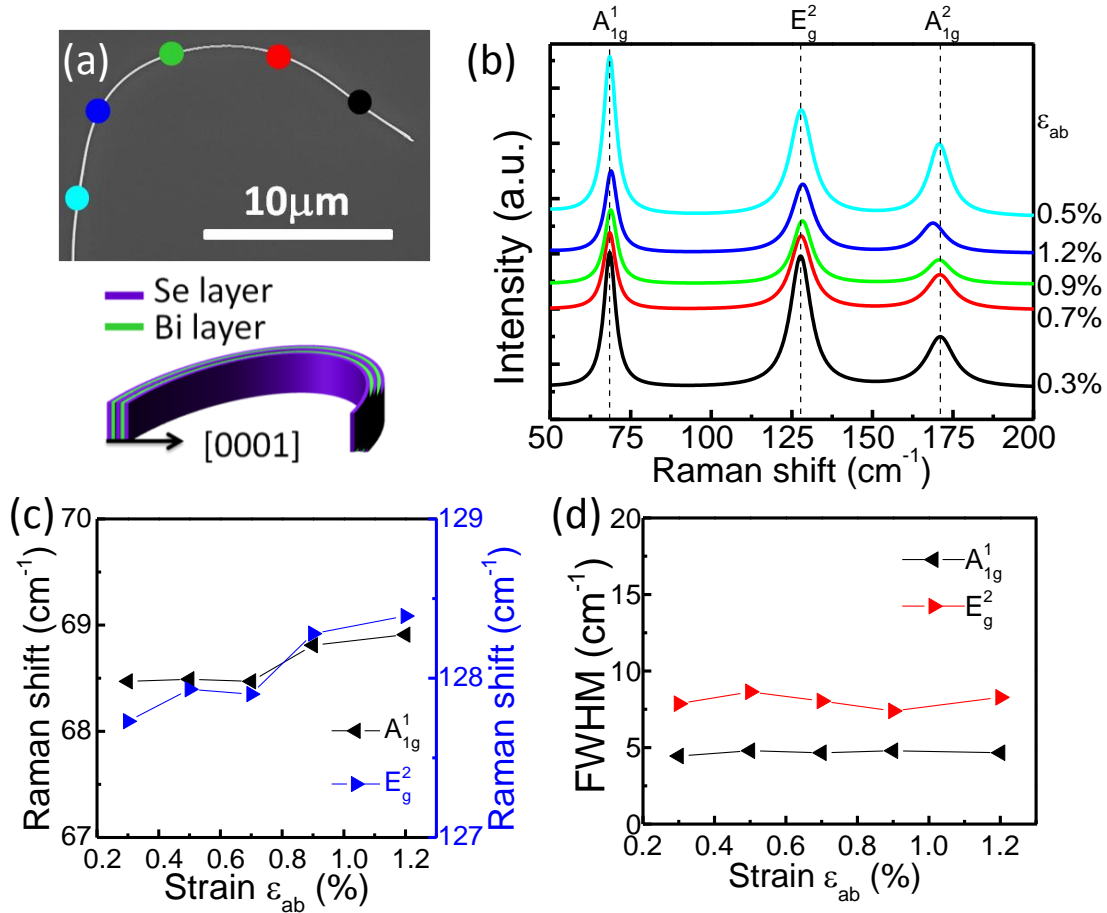
Figure S6. Raman spectra of a strained Bi_2Se_3 nanoribbon with the {0001} surface perpendicular to the substrate plane and the exposed {01$\bar{1}$5} top surface. (a) SEM image and schematic illustration of a bent Bi_2Se_3 nanoribbon with a thickness of 120 nm. (b) Lorentzian fitted Raman spectra collected at the different positions along the Bi_2Se_3 nanoribbon. The color of each curve corresponds to five different points on the Bi_2Se_3 nanoribbon. (c) Raman shift and (d) FWHM of A_{1g}^1 and E_g^2 modes *versus* strain.
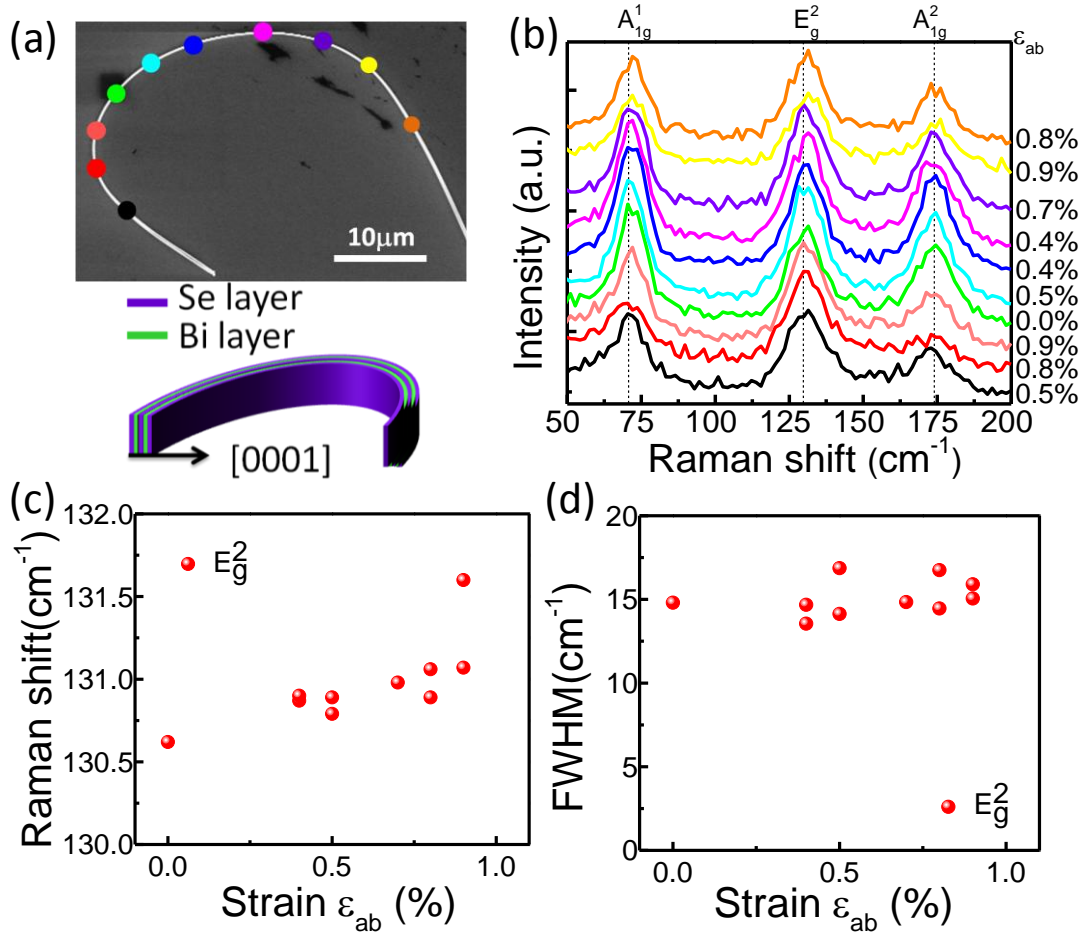
Figure S7. Raman spectra of a strained Bi_2Se_3 nanoribbon with the $\{0001\}$ surface perpendicular to the substrate plane and the exposed $\{01\bar{1}5\}$ top surface. (a) SEM image and schematic illustration of a bent Bi_2Se_3 nanoribbon with a thickness of 190 nm. (b) Raw Raman spectra collected at the different positions along the Bi_2Se_3 nanoribbon. The color of each curve corresponds to ten different points on the Bi_2Se_3 nanoribbon. (c) Raman shift and (d) FWHM of E_g^2 mode *versus* strain.